Energy & Environmental Science

ROYAL SOCIETY OF CHEMISTRY

PAPER

View Article Online
View Journal | View Issue

Cite this: *Energy Environ. Sci.*, 2024, **17**, 2260

Molecular modulation of nickel–salophen organic frameworks enables the selective photoreduction of CO_2 at varying concentrations†

Xiaohan Yu,‡[ab] Mingzi Sun,‡[c] Tianran Yan,[ab] Lin Jia,[ab] Mingyu Chu,[ab] Liang Zhang,[ab] Wei Huang,*[ab] Bolong Huang*[ce] and Yanguang Li*[abd]

Received 30th November 2023,
Accepted 5th February 2024

DOI: 10.1039/d3ee04121b

rsc.li/ees

Photocatalytic CO_2 reduction to value-added chemicals is appealing but challenging, especially under dilute CO_2 conditions. Herein, we present a molecular modulation strategy for porous metal–salophen organic frameworks (M-SOFs), involving cooperative regulation of the catalytically active metal centers and their local coordination environments for selective photocatalytic CO_2 reduction across a wide range of CO_2 concentrations. The optimal Ni-SOF shows a remarkable photocatalytic CO production rate of 16 908 μmol h^{-1} g^{-1} and near-unity selectivity under a pure CO_2 atmosphere, along with excellent structural stability. More impressively, it largely preserves the catalytic activity and selectivity even when exposed to dilute CO_2 (5–20 vol%). Both experimental and theoretical analyses support that the specific Ni–N_2O_2 coordination environment in the Ni-SOF endows it with strong CO_2 binding capacity. This, coupled with nanoporous skeletons, enhances local CO_2 enrichment and facilitates its subsequent conversion at the catalytic centers, thereby leading to superior photocatalytic performances at various CO_2 concentrations.

Broader context

Solar-driven CO_2 conversion has been considered as an ideal approach for reducing atmospheric CO_2 concentration while producing value-added chemicals and fuels. Over the past decades, tremendous progress has been made in the development of high-performance photocatalysts. Unfortunately, most of them are only operable under high-purity CO_2 conditions. Direct photoreduction of dilute CO_2 is appealing, given that industrial exhaust gases typically contain low concentrations of CO_2; however, it remains a formidable challenge. The key obstacles lie in the inadequate CO_2 capturing ability of the photocatalysts and unfavourable interactions between catalytic sites and CO_2 molecules. Here, we demonstrate the unique capability of metal–salophen organic frameworks – with properly engineered metal centers and coordination environments – to facilitate the local enrichment and subsequent conversion of CO_2. The optimal sample shows exceptional photocatalytic performance and near-unity CO_2-to-CO selectivity across a wide range of CO_2 concentrations.

Introduction

Excessive CO_2 emissions from fossil fuel combustion have been recognized as the dominant cause of global warming and climate change, posing a significant threat to our economic and environmental sustainability.[1] Several strategies have been proposed to reduce the atmospheric CO_2 concentration, either through physical sequestration or chemical conversion.[2,3] Among them, solar-driven CO_2 reduction to valuable chemicals (*e.g.*, CO, CH_4, CH_3OH, and HCOOH) offers a particularly attractive approach by transforming solar energy into chemical energy while neutralizing CO_2 emissions.[4,5] Nevertheless, current investigations are primarily based on pure CO_2 feedstocks. Given that a major source of CO_2 emissions is industrial exhaust gases which contain relatively low CO_2 concentrations typically in the range of 5–20%, the direct conversion of low-concentration CO_2 is more practically relevant and highly

[a] *Institute of Functional Nano & Soft Materials (FUNSOM), Soochow University, Suzhou, 215123, China. E-mail: weihuang@suda.edu.cn, yanguang@suda.edu.cn*
[b] *Jiangsu Key Laboratory for Advanced Negative Carbon Technologies, Soochow University, Suzhou 215123, China*
[c] *Department of Applied Biology and Chemical Technology, The Hong Kong Polytechnic University, Hung Hom, Kowloon, Hong Kong SAR 999077, China. E-mail: bhuang@polyu.edu.hk*
[d] *Macao Institute of Materials Science and Engineering (MIMSE), MUST-SUDA Joint Research Center for Advanced Functional Materials, Macau University of Science and Technology, Taipa 999078, Macau SAR, China*
[e] *Research Centre for Carbon-Strategic Catalysis, The Hong Kong Polytechnic University, Hung Hom, Kowloon, Hong Kong SAR 999077, China*

† Electronic supplementary information (ESI) available. See DOI: https://doi.org/10.1039/d3ee04121b

‡ These two authors contribute equally.

desirable.[6] Unfortunately, limited attempts so far have shown that diluted CO_2 concentrations usually compromise the activity and/or selectivity.[7] This is mainly attributed to inefficient CO_2 capture and unfavorable binding interactions between catalytic sites and substrates.[8] As a result, the rational design of photocatalysts with optimized catalytic centers and CO_2 binding capacity is crucial.

In nature, enzymes can catalyze complicated redox reactions with high activity and specificity towards target products.[9] Their active sites are typically composed of metal cations bound to the amino acid residues of the proteins containing nitrogen (N), sulfur (S), and oxygen (O) atoms. For instance, galactose oxidase is a well-known mononuclear oxidoreductase, in which the Cu center is ligated by two pyrrolic N atoms and two phenolic O atoms.[10] Such a Cu–N_2O_2 site can efficiently catalyze the two-electron oxidation of primary alcohols to corresponding aldehydes. Inspired by these biocatalysts, great efforts have been devoted to exploiting artificial enzymes in order to mimic the functions of natural molecules.[11–14] Salen or salophen compounds are a type of Schiff-base ligands with planar tetradentate N_2O_2 sites, capable of accommodating various transition metal ions.[15] By judiciously varying metal catalytic centers and ancillary organic ligands, it is possible to fine-tune their catalytic performances. Benefiting from their structural diversity and easy accessibility, metal–salen/salophen complexes have been widely used as enzyme mimics for different catalytic reactions.[16,17] Nevertheless, their potential in photocatalytic CO_2 reduction has not been explored. This may be partly attributed to the unsatisfactory long-term stability of molecular salen/salophen catalysts during photocatalytic reactions as a result of their aggregation or degradation.[18]

Immobilizing molecular catalysts onto suitable porous hosts offers a potential solution to the above issue. Previous investigations have demonstrated that porous skeletons could enhance the robustness of catalytic sites, and facilitate the enrichment of CO_2 molecules in their vicinity.[19,20] This is of great significance for durable and efficient CO_2 conversion, particularly under diluted CO_2 concentrations.

To this end, here we synthesize a new type of metal–salophen organic framework (M-SOF, M = Co, Ni, Cu, and Zn) by covalently incorporating metal–salophen nodes into porous architectures for the efficient and durable photoreduction of CO_2 at varying concentrations. By tuning the predesigned organic precursors and metal species, the activity and CO selectivity of the resulting catalysts could be readily modulated. Of particular note is that the Ni-SOF containing Ni–N_2O_2 centers is the most photocatalytically active; across a wide range of CO_2 concentrations (5–100 vol%), it exhibits an extremely high photocatalytic activity of up to 16 908 μmol h^{-1} g^{-1} and near-unity selectivity for CO production. Experimental and theoretical studies show that the outstanding catalytic activity of the Ni-SOF originates from its porous frameworks and favorable binding towards CO_2 and reaction intermediates.

Results and discussion

Fig. 1a schematically illustrates the synthetic procedure of Ni-SOFs *via* a metal-template-assisted Schiff-base reaction between salicylaldehyde and 1,3,5-tris(4-aminophenyl)triazine (TAPT) in *N*,*N*-dimethylformamide (DMF). During the synthesis, salicylaldehyde and nickel acetate were first mixed in DMF at room temperature to form a soluble O-coordinated Ni intermediate (Ni–O_4), as evidenced by the change in solution color from light green to yellow.[21] The subsequent addition of TAPT initiated the condensation reaction with the aldehyde functionalities of Ni–O_4 at elevated temperatures and ultimately gave rise to an extended coordination polymer with Ni–N_2O_2 nodes. It is worth noting that such a stepwise synthetic procedure is crucial in order to achieve the desired metal–N_2O_2 coordination. TAPT is employed as the building block because of its nitrogen-rich composition, which would result in nitrogen-rich porous skeletons to facilitate CO_2 capture. Other samples with different metal centers (Co-SOFs, Cu-SOFs, and Zn-SOFs) were synthesized by adding corresponding metal salts under otherwise identical conditions. To investigate the effect of coordination environments on photocatalysis, N-coordinated Ni–N_4, and N/S-coordinated Ni–N_2S_2 were also synthesized by replacing salicylaldehyde with 2-pyridinecarboxaldehyde and 2-mercaptobenzaldehyde, respectively.

The chemical structures of our samples were first interrogated by Fourier transform infrared (FT-IR) and X-ray photoelectron spectroscopy (XPS). For the sake of clarity, the following discussion will be focused on Ni-SOF as a representative unless otherwise specified. From its FT-IR spectrum, the successful condensation between salicylaldehyde and TAPT is evidenced by the disappearance of the $-NH_2$ stretching vibrations at 3209 and 3321 cm^{-1} as well as the emergence of a new peak at 1621 cm^{-1} attributed to –CH═N (Fig. S1, ESI†).[22] The presence of two peaks at 1361 and 1508 cm^{-1}, characteristic of triazine, also signifies the incorporation of TAPT within the coordination networks.[23] Moreover, two weak bands corresponding to Ni–O and Ni–N are observed at 589 and 458 cm^{-1}, respectively.[24] They suggest that the coordination nodes in Ni-SOF are formed through the interactions between Ni cations and surrounding imine/hydroxyl groups. Fig. S2 (ESI†) summarizes the XPS results of Ni-SOFs. The N 1s spectrum of the Ni-SOF could be deconvoluted into three peaks assigned to pyridinic N in the triazine unit (398.0 eV), C═N (398.8 eV) and Ni–N (399.8 eV).[22] Its O 1s spectrum shows two peaks at 528.3 and 531.6 eV, corresponding to Ni–O and C–O, respectively.[25] The Ni center in the Ni-SOF is determined to be in the divalent state based on its Ni 2p spectrum.[26]

The electronic state and coordination environment of the Ni-SOF were further examined by synchrotron X-ray absorption spectroscopy (XAS). Fig. 1b illustrates its X-ray absorption near-edge structure (XANES) spectrum at the Ni K-edge. The white-line peak of Ni-SOFs is similar to that of NiO, corroborating the divalent state of Ni centers in Ni-SOFs. The corresponding Fourier transform extended X-ray absorption fine structure (EXAFS) spectrum of Ni-SOFs exhibits a prominent peak at 1.60 Å, which is a value between the bonding length of Ni–N in nickel phthalocyanine (NiPc) (1.46 Å) and that of Ni–O in NiO (1.65 Å) (Fig. 1c). This again supports the mixed Ni–N/O first-shell coordination.[27] No Ni–Ni scattering is observed,

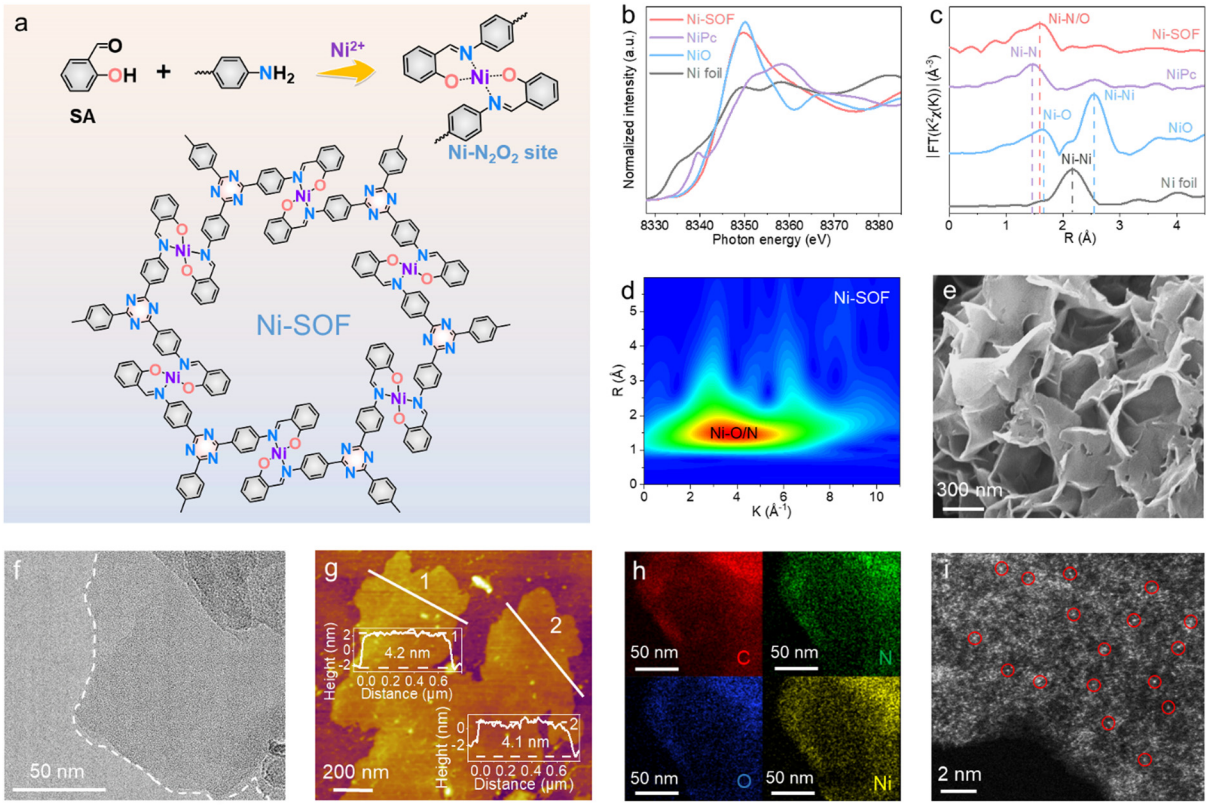

Fig. 1 Synthesis and characterizations of Ni-SOFs. (a) Schematic illustration of the synthetic procedure of Ni-SOFs. (b) XANES and (c) EXAFS spectra of Ni-SOFs, NiPc, NiO and Ni foil. (d) Wavelet transform of the EXAFS spectra of Ni-SOFs. (e) SEM, (f) TEM, (g) AFM, (h) EDS elemental mapping and (i) HAADF-STEM images of Ni-SOFs.

confirming the atomic dispersion of Ni^{2+} cations in Ni-SOFs. Further evidence is obtained from the wavelet transform (WT) of the EXAFS spectra (Fig. 1d and Fig. S3, ESI†). The maximum WT position of Ni-SOFs apparently differs from those of Ni–N in NiPc and Ni–O in NiO, but partially overlaps with them.

To fully unveil the steric structure of Ni–N_2O_2 nodes in Ni-SOFs, a model molecule (denoted as Ni–salophen) was synthesized as its mimic and analyzed by single-crystal X-ray diffraction (XRD) measurement (Fig. S4 and Table S1, ESI†). It is shown to possess a four-coordinated Ni center with the first coordination sphere consisting of two phenolic O atoms and two imine N atoms. The bond length of Ni–O is calculated to be 1.83 Å, slightly shorter than that of Ni–N (1.91 Å) as a result of the higher electronegativity of O atoms. Two pairs of *trans*-coordinated O and N atoms around the central Ni atom form a nearly planar rhomboid geometry owing to the small differences in bond lengths and bond angles. It is believed that such an open metal center with exposed axial coordination is advantageous for CO_2 binding and activation.[28]

Scanning electron microscopy (SEM) and transmission electron microscopy (TEM) imaging show that the Ni-SOF consists of crumpled and stacked nanosheets (Fig. 1e and f). Individual nanosheets are estimated to have a size ranging from 200 nm to 1 μm. From atomic force microscopy (AFM) height profiles at multiple locations, the nanosheet thickness is measured to be approximately 4 nm (Fig. 1g). Such an ultrathin nanosheet geometry is desirable for catalytic applications as it promotes the exposure of inner active sites and maximizes atom utilization. Energy dispersive X-ray spectroscopy (EDS) mapping under scanning transmission electron microscopy (STEM) reveals the uniform distribution of C, N, O and Ni on Ni-SOF nanosheets (Fig. 1h). The aberration-corrected high-angle annular dark-field STEM (HAADF-STEM) image shows discrete bright spots (some marked with red circles) corresponding to heavy Ni atoms, corroborating the atomic dispersion of Ni sites throughout the examined region (Fig. 1i). Moreover, the Ni content in Ni-SOFs is found to be 10.5 wt% as analyzed by inductively coupled plasma mass spectrometry (ICP-MS), which is in good agreement with the theoretical value (10.2 wt%). N_2 isotherm sorption measurements show that the Ni-SOF has a specific surface area of 116 $m^2\ g^{-1}$ (Fig. S5, ESI†). In addition to Ni-SOFs, the structures of other samples with different metal sites and coordination environments were also characterized, and results are summarized in the ESI† (Fig. S6–S8 and Table S2).

We evaluated the photocatalytic performance of our samples under pure CO_2. The reactions were conducted in a mixed solution of acetonitrile and water under visible light irradiation ($\lambda > 420$ nm) using $[Ru(bpy)_3]Cl_2$ as the photosensitizer and triisopropanolamine (TIPA) as the hole scavenger. Gaseous products (*e.g.*, CO and H_2) were analyzed and quantified by gas chromatography (GC) based on their calibration curves (Fig. S9, ESI†). We explored different solvent ratios, catalyst

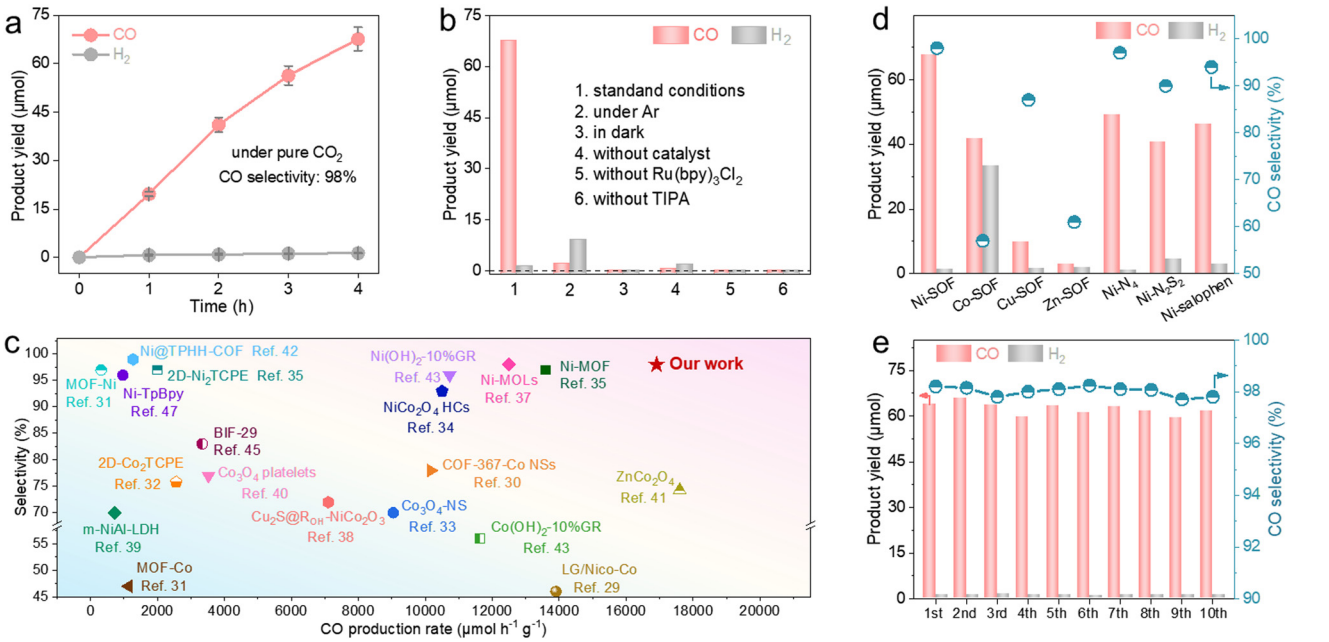

Fig. 2 Photocatalytic performance of Ni-SOFs under pure CO_2. (a) Time-dependent CO and H_2 production on Ni-SOFs. (b) Control experiments conducted under different conditions. (c) Performance comparison of Ni-SOFs with other organic or inorganic catalysts in terms of the CO production rate and selectivity under pure CO_2. (d) CO production and selectivity of different samples. (e) Cycling tests of Ni-SOFs.

concentrations, and hole scavengers (Fig. S10, ESI†). Under the optimized conditions, the Ni-SOF exhibits an almost linear accumulation of CO over time and yields a total of 67.6 μmol of CO after 4 h irradiation (Fig. 2a). This corresponds to an average mass-specific CO evolution rate of 16 908 μmol h^{-1} g^{-1}. Its maximum apparent quantum efficiency (AQE) toward CO production is 2.8% at 450 nm (Fig. S11, ESI†). The isotope experiment using $^{13}CO_2$ provides evidence that CO stems from CO_2 photoreduction rather than other organic substances or the catalyst itself (Fig. S12, ESI†). Control experiments also show that negligible CO is produced in the absence of light, CO_2, Ni-SOF, photosensitizer or hole scavenger under otherwise identical conditions (Fig. 2b). In addition to CO, only a trace amount of H_2 (1.3 μmol) is measured on Ni-SOFs, and no liquid products (such as formic acid or methanol) are detected in the reaction solution by nuclear magnetic resonance (NMR) spectroscopy (Fig. S13, ESI†). As a result, a high CO selectivity of 98% is achieved for our catalyst. It is worth highlighting that the great activity and selectivity measured for our Ni-SOF places it at the top of other organic competitors including covalent organic frameworks (COFs) and metal–organic frameworks (MOFs) as well as most inorganic counterparts (Fig. 2c and Table S3, ESI†).[29–47] In particular, its mass-specific CO production rate is about 17.5 and 8.5 times larger than those of the state-of-the-art COF catalyst (Ni-TpBpy) and MOF catalyst (2D-Ni_2TCPE), respectively.[32,47] We are aware that higher mass-specific rates have been reported for some transition metal oxides, but their selectivity for carbonaceous products was generally lower than 80%.[41]

The catalytic performances of coordinated metal centers are greatly impacted by not only the metal identities but also their local chemical environments (Fig. 2d). Under identical reaction conditions, the Co-SOF shows a significantly decreased CO production rate of 10 157.5 μmol h^{-1} g^{-1} and a higher H_2 evolution activity of 8322.5 μmol h^{-1} g^{-1}, leading to a low CO selectivity of 57%. Even though the Cu-SOF demonstrates a good CO selectivity (87%), its CO production rate is 7 times lower than that of Ni-SOFs. The Zn-SOF exhibits the lowest CO production rate of 695 μmol h^{-1} g^{-1} and a moderate CO selectivity of 61%. Moreover, the substitution of O atoms in the first coordination sphere of Ni-SOFs with less electronegative N or S (Ni–N_4 and Ni–N_2S_2, respectively) leads to noticeable decreases in both the activity and selectivity, and their measured activities are found to correlate with the electronegativity of coordinating elements. The above results suggest the critical roles of metal centers and their coordination environments during CO_2 photoreduction. The Ni-SOF featuring Ni–N_2O_2 active sites represents the optimal combination to enable active and selective CO_2 photoreduction to CO. In addition, despite having identical Ni–N_2O_2 catalytic sites, the Ni-SOF is more active than Ni–salophen, presumably due to its porous microstructure which enriches local CO_2 concentration.[48]

Stability is another important performance metric of photocatalysts. Here, we carried out long-term photocatalysis as shown in Fig. S14 (ESI†). The CO production rate of the Ni-SOF gradually decreases and reaches a plateau after 5 h. However, its activity can be completely restored when fresh $[Ru(bpy)_3]^{2+}$ is replenished. This observation suggests that the performance decay is due to the degradation of the photosensitizer rather than the Ni-SOF.[49] In contrast, Ni–salophen experiences an irreversible activity loss after about 5 h. It underlines the evident advantage of metal–salophen organic

frameworks with improved structural robustness and catalytic stability. The excellent stability of Ni-SOFs is also supported by the cycling experiment showing no noticeable performance loss after a total of 40 h illumination (Fig. 2e). In addition, the ICP-MS analysis of the reaction filtrate after the cycling test reveals a negligible Ni concentration (0.264 ppm), thus ruling out the possibility of Ni leaching out of Ni-SOFs during photocatalysis. Spectroscopic and microscopic analyses of the recovered Ni-SOF disclose no discernable structural changes (Fig. S15, ESI†).

Effective charge transfer from the photosensitizer to the catalytic sites is a prerequisite for initiating redox reactions. To probe the charge transfer behavior between $[Ru(bpy)_3]^{2+}$ and Ni-SOFs, steady-state and time-resolved photoluminescence (PL) spectroscopy studies were conducted. As shown in Fig. S16 (ESI†), the steady-state PL peak intensity of $[Ru(bpy)_3]^{2+}$ gradually decreases as the Ni-SOF concentration increases, while the TIPA concentration has no significant effect on the PL intensity. Corresponding Stern–Volmer plots show the much higher quenching efficiency of Ni-SOFs than TIPA. These results reveal that the electron transfer from the photosensitizer to the catalyst is the initial step of the photocatalytic cycle.[32] The time-resolved PL spectrum of $[Ru(bpy)_3]^{2+}$ follows a single exponential decay with an average PL lifetime of 237 ns, consistent with literature results (Fig. 3a).[50] In the presence of Ni-SOFs, a double-exponential decay is observed with fitted lifetimes of 0.49 ns and 225 ns (Fig. 3b). The former is attributed to the charge transfer between $[Ru(bpy)_3]^{2+}$ and Ni-SOFs. Compared to those measured in the presence of other M-SOFs (M = Co, Cu, and Zn), the shorter lifetime observed with Ni-SOFs at the early stage suggests more efficient electron transfer (Fig. S17, ESI†).[51] Moreover, electron paramagnetic resonance (EPR) spectroscopy was conducted (Fig. 3c). Upon irradiation, a sharp EPR signal ascribed to Ni^+ is observed at g = 2.06,[52] while it becomes significantly attenuated upon CO_2

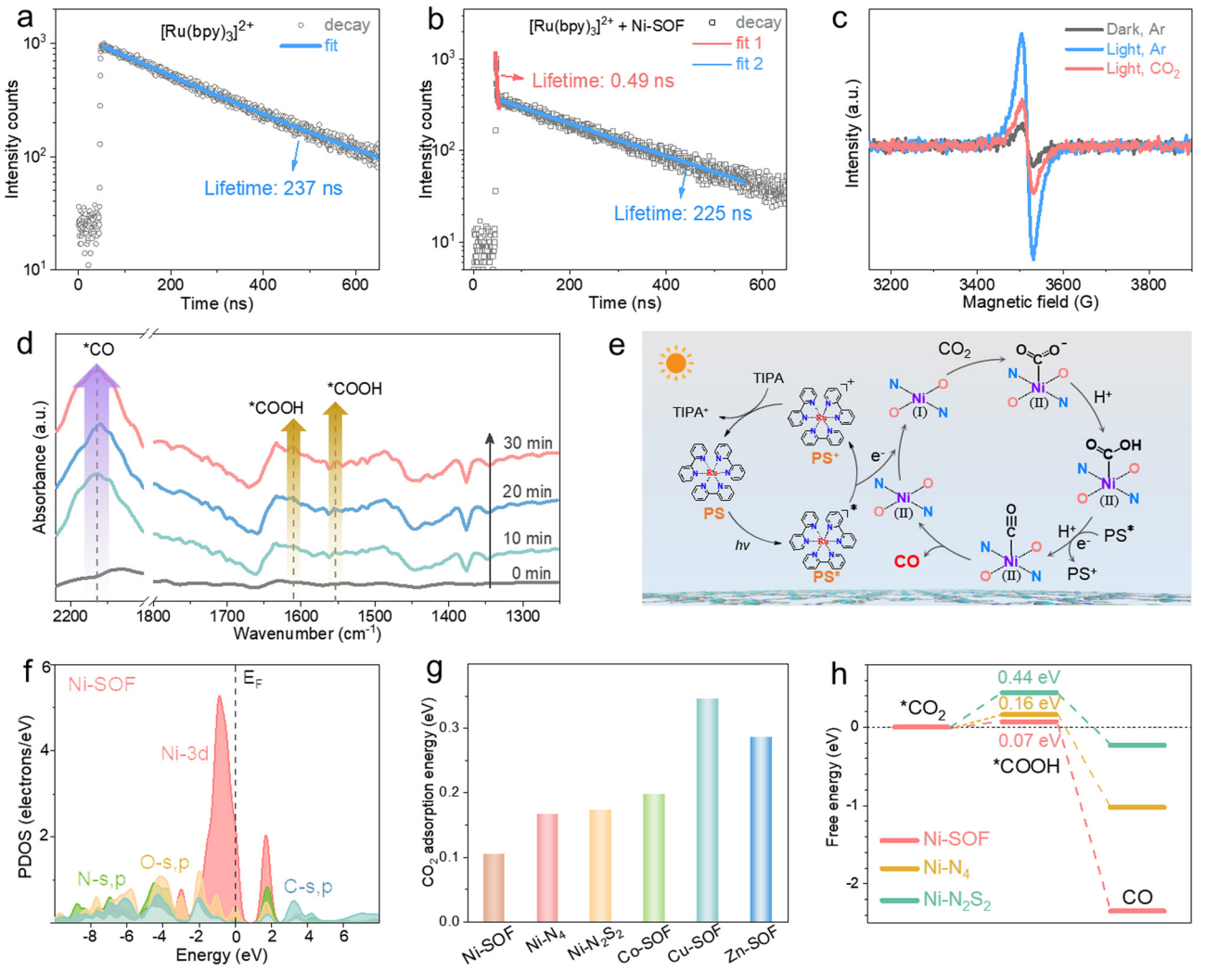

Fig. 3 Charge transfer kinetics and possible reaction mechanism. (a) and (b) Time-resolved PL spectra of (a) $[Ru(bpy)_3]Cl_2$ and (b) $[Ru(bpy)_3]Cl_2$ + Ni-SOF in acetonitrile. (c) EPR spectra of Ni-SOFs under different conditions. (d) *Operando* DRIFTS spectra of Ni-SOFs under irradiation for different durations of time. (e) Schematic illustration of the proposed catalytic cycle. (f) PDOS spectra of Ni-SOFs. (g) CO_2 adsorption energy on different catalysts. (h) Calculated free energy of CO_2 photoreduction on Ni sites with different coordination environments.

introduction. Considering that Ni^{2+} is EPR-silent, this observation indicates that Ni^{2+} sites can readily accept electrons from the excited photosensitizer, and subsequently transfer them to CO_2 to initiate the reduction reaction. The CO_2 reduction process was then be tracked by *in situ* diffuse reflectance infrared Fourier transform spectroscopy (DRIFTS). Fig. 3d clearly shows the vibration bands from intermediates within a 30-minute irradiation period. The two peaks at 1611 and 1552 cm^{-1} are characteristic of the *COOH intermediate, and their peak intensity increases as the irradiation continues.[53] In the meantime, a pronounced *CO adsorption peak at 2163 cm^{-1} is also observed, indicating a high *CO surface coverage under irradiation.[54]

Based on the above spectroscopic results, a possible mechanism for CO_2 photoreduction is proposed and illustrated in Fig. 3e. Upon visible light irradiation, $[Ru(bpy)_3]^{2+}$ (PS) is promoted to its excited state (PS*). Subsequently, photoexcited electrons are transferred to the Ni^{2+} sites of Ni-SOFs within a short time scale, generating catalytically active Ni^{+} centers. The oxidized photosensitizer (PS^{+}) is then reduced back to its ground state by accepting electrons from TIPA. Electrons located on the Ni^{+} centers are further transferred to absorbed CO_2, initiating the reduction reaction which involves the sequential formation of *COOH and *CO intermediates. At the end, *CO desorbs from the catalyst surface, thus stopping the reaction cycle.

To gain more insights into the catalytic mechanism, density functional theory (DFT) calculations were performed. The electronic distribution diagrams of Ni-SOFs, $Ni–N_4$, and $Ni–N_2S_2$ near the Fermi level (E_F) are depicted in Fig. S18 (ESI†). The maximum bonding orbital distribution is located closer to Ni in Ni-SOFs compared to those in $Ni–N_4$ and $Ni–N_2S_2$, suggesting the electron-rich feature of Ni sites in Ni-SOFs. The electronic modulation of metal centers by the coordination environment is evident from the projected partial density of states (PDOS) analysis. As shown in Fig. 3f, the Ni-3d orbitals of Ni-SOFs

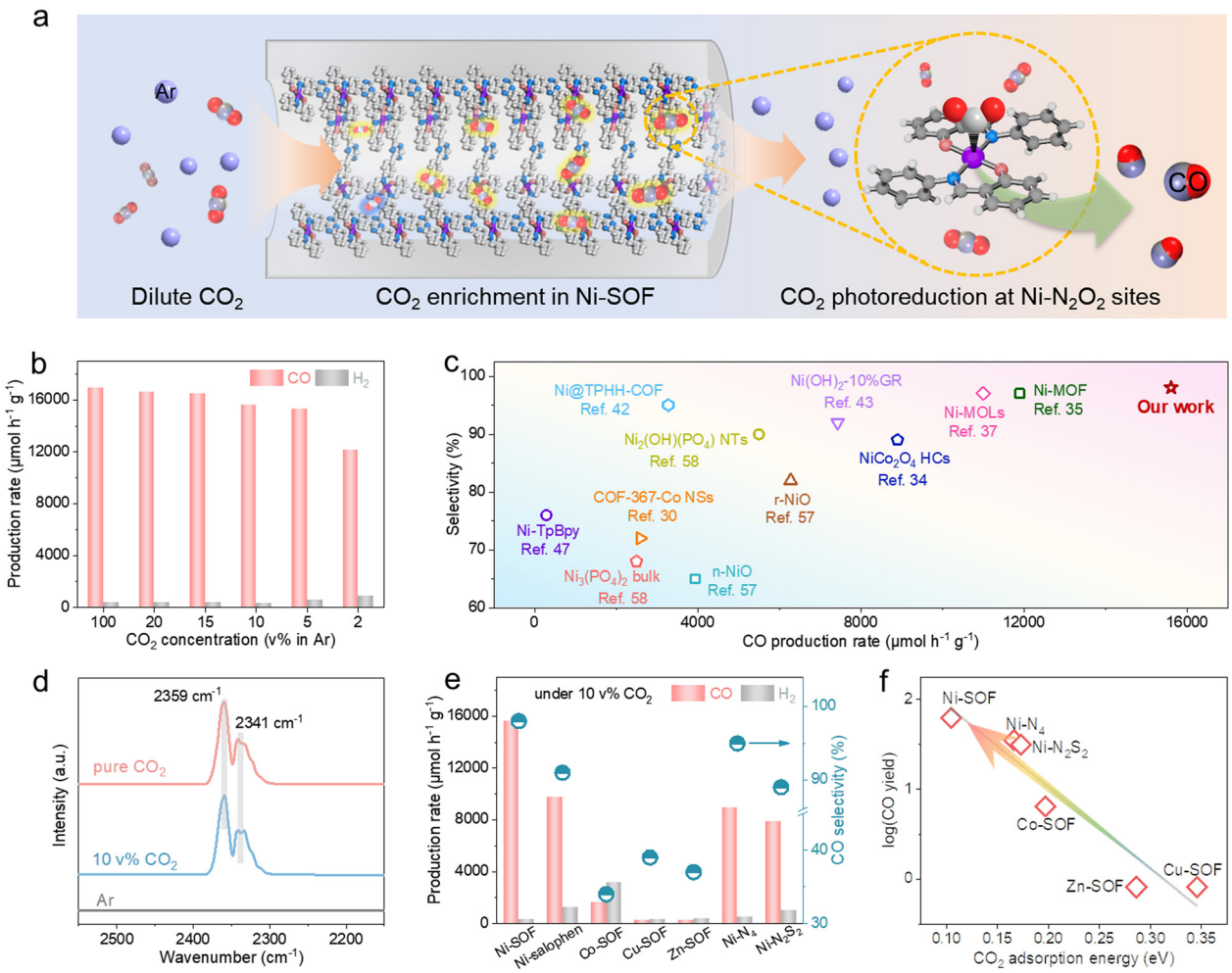

Fig. 4 Performance evaluation of the catalysts under dilute CO_2. (a) Schematic illustration of the enrichment and photoreduction of dilute CO_2 in Ni-SOFs. (b) Photocatalytic activities of Ni-SOFs at various CO_2 concentrations. (c) Performance comparison of Ni-SOFs with other organic or inorganic catalysts in terms of the CO production rate and selectivity under 10 vol% CO_2 in Ar. (d) DRIFTS spectra of Ni-SOFs in pure Ar, pure CO_2 or 10 vol% CO_2 atmospheres. (e) CO production rate and selectivity of different catalysts under 10 vol% CO_2. (f) Correlation between the logarithm of the CO production rate on different catalysts under 10 vol% CO_2 and their CO_2 adsorption energy.

exhibit a sharp peak near E_F at E_v −0.88 eV (E_v = 0 eV). The s, p orbitals of O and N sites have good overlaps with the Ni-3d orbitals, indicating their strong binding interactions with central Ni atoms are necessary for the formation of a stable coordination configuration and efficient site-to-site electron transfer.[55] By comparison, the metallic 3d orbitals of other catalysts (Ni–N_4, Ni–N_2S_2, Co–N_2O_2, Cu–N_2O_2, and Zn–N_2O_2) are located at more negative positions related to their E_F with obviously decreased overlaps with the s and p orbitals of surrounding heteroatoms (Fig. S19, ESI†). The d-band center and optical absorption comparisons also confirm the improved catalytic activity and optical properties of Ni-SOFs to promote the photocatalytic performances of CO_2 reduction (Fig. S20, ESI†).

Furthermore, CO_2 adsorption energies on different catalysts were calculated and compared (Fig. 3g). The Ni-SOF has the lowest adsorption energy, suggesting its strongest binding with CO_2. This result is corroborated by the temperature programmed CO_2 desorption (TPD) measurements showing that the Ni-SOF has the largest CO_2 desorption capacity and highest desorption temperature (Fig. S21, ESI†). Favorable CO_2 binding ability is believed to be conducive to CO_2 capture and enrichment around the catalytic sites, thereby accelerating CO_2 conversion.[56] In addition, the free energy profiles of different catalysts during CO_2 reduction were simulated. The conversion from *CO_2 to *COOH is found to be the rate-determining step (RDS) for all the catalysts (Fig. 3h and Fig. S22, ESI†). Among them, the Ni-SOF shows the smallest energy barrier of 0.07 eV, indicating that the redox reaction on the Ni-SOF is the most favorable. Further conversion from *COOH to CO is exothermic and thereby spontaneous once *COOH is formed.

Encouraged by the great catalytic capacity and favorable CO_2 binding of the Ni-SOF, we moved on to assess its catalytic performance at dilute CO_2 concentrations. Fig. 4a schematically illustrates the local enrichment and subsequent photoreduction of diluted CO_2 within the porous skeletons of Ni-SOFs. As demonstrated in Fig. 4b and Fig. S23 (ESI†), the Ni-SOF exhibits an exceptional catalytic performance at varying CO_2 concentrations. Both the CO production rate and selectivity remain largely stable across a wide range of CO_2 concentrations from 5 to 20 vol% in Ar. At a CO_2 concentration as low as 2 vol%, the mass-specific CO production rate is measured to be 12 100 μmol h^{-1} g^{-1}, retaining 72% of the value achieved under pure CO_2 as well as a high CO selectivity of 93%. Moreover, the AQE value at 10 vol% CO_2 is 2.7% at 450 nm, which is very close to that obtained under pure CO_2 (2.8%) (Fig. S24, ESI†). To the best of our knowledge, such high activity and selectivity have rarely been achieved before under dilute CO_2 (Fig. 4c and Table S4, ESI†),[37,43,57,58] exceeding those of other organic and inorganic candidates, even measured under pure CO_2.[34,42] The DRIFTS spectra of Ni-SOFs under pure and diluted (10 vol%) CO_2 show two identical absorption bands at 2359 and 2341 cm^{-1}, assigned to adsorbed CO_2 with the end-on configuration (Fig. 4d).[59] Importantly, their peak intensity and integrated areas are found to be largely independent of the CO_2 concentration. This implies that Ni-SOFs can enrich local CO_2 concentration when the feedstock becomes much diluted and may rationalize the exceptional photocatalytic activity measured under low-concentration CO_2.

The great photocatalytic performance under low-concentration CO_2 appears to be unique to Ni-SOFs. Ni–salophen presents considerably lower activity despite its similar coordination environment with Ni-SOFs (Fig. 4e). Replacing the central Ni with Co results in a decreased mass-specific activity of 2167 μmol h^{-1} g^{-1} (more than 4 times lower than that under pure CO_2 on Co-SOFs) and low CO selectivity of 34%. More strikingly, CO_2 photoreduction on Cu-SOFs and Zn-SOFs becomes almost quenched under the same conditions. Furthermore, both Ni–N_4 and Ni–N_2S_2 exhibit about half of the activity of Ni-SOFs under 10 vol% CO_2. We note that the measured activity here is roughly correlated with the CO_2 binding energy predicted in Fig. 4f. The strongest binding affinity of Ni-SOF affords our catalyst with the most appealing activity by enriching CO_2 local concentration and facilitating its subsequent conversion.

Conclusions

In summary, we synthesized a new class of M-SOF materials *via* facile metal-assisted Schiff-base reactions for efficient photocatalytic CO_2 reduction. All the samples are composed of atomically dispersed metal sites and controlled local coordination environments, both of which could be precisely modulated *via* varying the predesigned organic moieties and metal species. The optimal sample, the Ni-SOF with Ni–N_2O_2 nodes, showed the highest CO production rate of 16 908 μmol h^{-1} g^{-1} with an excellent selectivity up to 98%. Impressively, the Ni-SOF was able to maintain its photocatalytic performance across a wide range of CO_2 concentrations (5–20 vol% in Ar) without reducing the selectivity. Experimental and theoretical studies revealed that the superior catalytic performance of Ni-SOFs mainly originated from the favorable d-band electronic modulation of the coordinated Ni atoms and optimal binding strength with the intermediates. In particular, the strong CO_2 affinity of Ni-SOFs is identified as the key factor for the efficient conversion of diluted CO_2. Our study demonstrates a promising strategy for rationalizing the chemical and electronic configurations of metal catalytic centers toward the direct utilization of diluted CO_2 from industrial exhaust gas.

Author contributions

Y. L. and W. H. conceived the project and designed the experiments. X. Y. synthesized the catalysts and conducted the structure analysis and photocatalytic tests. B. H. and M. S. performed the theoretical calculations. T. Y. and L. Z. conducted the X-ray absorption measurements. L. J. carried out TEM characterization studies. M. C. performed TPD measurements. X. Y., M. S., W. H., B. H., and Y. L. co-wrote the paper. All authors discussed the results and commented on the manuscript.

Conflicts of interest

There are no conflicts to declare.

Acknowledgements

We acknowledge the financial support received from the National Key R&D Program of China (2021YFA1501101), the National Natural Science Foundation of China (22002100, U2002213, and 52161160331), the National Natural Science Foundation of China/Research Grant Council of Hong Kong Joint Research Scheme (N_PolyU502/21), the National Natural Science Foundation of China/Research Grants Council of Hong Kong Collaborative Research Scheme (CRS_PolyU504/22), the Natural Science Foundation of Jiangsu Province (BK20220027), the Natural Science Foundation of the Jiangsu Higher Education Institutions of China (20KJA430002), the Science and Technology Development Fund Macau SAR (0077/2021/A2), the Collaborative Innovation Center of Suzhou Nano Science and Technology, and the funding for Projects of Strategic Importance of The Hong Kong Polytechnic University (Project Code: 1-ZE2V), the Shenzhen Fundamental Research Scheme-General Program (JCYJ20220531090807017), the Natural Science Foundation of Guangdong Province (2023A1515012219) and Departmental General Research Fund of The Hong Kong Polytechnic University (Project Code: ZVUL). We thank the Shanghai Synchrotron Radiation Facility (beamline 11B) for the allocation of synchrotron beamtime, Dr Jie Xu for HAADF-STEM characterization and Chunpeng Wu for DRFITS measurements. B. H. is also grateful for the support provided by the Research Centre for Carbon-Strategic Catalysis (RC-CSC), the Research Institute for Smart Energy (RISE), and the Research Institute for Intelligent Wearable Systems (RI-IWEAR) of the Hong Kong Polytechnic University.

Notes and references

1 D. Campbell-Lendrum, T. Neville, C. Schweizer and M. Neira, *Nat. Med.*, 2023, **29**, 1631–1638.
2 C. J. Nielsen, H. Herrmann and C. Weller, *Chem. Soc. Rev.*, 2012, **41**, 6684–6704.
3 J. Wu, Y. Huang, W. Ye and Y. Li, *Adv. Sci.*, 2017, **4**, 1700194.
4 E. Gong, S. Ali, C. B. Hiragond, H. S. Kim, N. S. Powar, D. Kim, H. Kim and S.-I. In, *Energy Environ. Sci.*, 2022, **15**, 880–937.
5 W. Huang, W. Luo and Y. Li, *Mater. Today*, 2020, **40**, 160–172.
6 T. Nakajima, Y. Tamaki, K. Ueno, E. Kato, T. Nishikawa, K. Ohkubo, Y. Yamazaki, T. Morimoto and O. Ishitani, *J. Am. Chem. Soc.*, 2016, **138**, 13818–13821.
7 Y. Yamazaki, M. Miyaji and O. Ishitani, *J. Am. Chem. Soc.*, 2022, **144**, 6640–6660.
8 X. Wu, Y. Li, G. Zhang, H. Chen, J. Li, K. Wang, Y. Pan, Y. Zhao, Y. Sun and Y. Xie, *J. Am. Chem. Soc.*, 2019, **141**, 5267–5274.
9 S. Bierbaumer, M. Nattermann, L. Schulz, R. Zschoche, T. J. Erb, C. K. Winkler, M. Tinzl and S. M. Glueck, *Chem. Rev.*, 2023, **123**, 5702–5754.
10 A. John, M. M. Shaikh and P. Ghosh, *Dalton Trans.*, 2008, 2815–2824.
11 H. Huang, X. Jing, J. Deng, C. Meng and C. Duan, *J. Am. Chem. Soc.*, 2023, **145**, 2170–2182.
12 M. Vázquez-González, Z. Zhou, Y. Biniuri, B. Willner and I. Willner, *Biochemistry*, 2021, **60**, 956–965.
13 A. A. Shteinman, *Catalysts*, 2023, **13**, 415.
14 Z. Wang, P. Yeary, X. Feng and W. Lin, *J. Am. Chem. Soc.*, 2023, **145**, 8647–8655.
15 J. Zhang, L. Xu and W.-Y. Wong, *Coord. Chem. Rev.*, 2018, **355**, 180–198.
16 C. J. Whiteoak, G. Salassa and A. W. Kleij, *Chem. Soc. Rev.*, 2012, **41**, 622–631.
17 S. Signorella, C. Palopoli and G. Ledesma, *Coord. Chem. Rev.*, 2018, **365**, 75–102.
18 C.-B. Li, Y. Chu, J. He, J. Xie, J. Liu, N. Wang and J. Tang, *ChemCatChem*, 2019, **11**, 6324–6331.
19 V. Mouarrawis, R. Plessius, J. I. van der Vlugt and J. N. H. Reek, *Front. Chem.*, 2018, **6**, 623.
20 M. Lu, M. Zhang, J. Liu, Y. Chen, J.-P. Liao, M.-Y. Yang, Y.-P. Cai, S.-L. Li and Y.-Q. Lan, *Angew. Chem., Int. Ed.*, 2022, **61**, e202200003.
21 N. Zhao, K. Cai and H. He, *Dalton Trans.*, 2020, **49**, 11467–11479.
22 H. Zhang, Z. Lin, P. Kidkhunthod and J. Guo, *Angew. Chem., Int. Ed.*, 2023, **62**, e202217527.
23 L. Chen, L. Wang, Y. Wan, Y. Zhang, Z. Qi, X. Wu and H. Xu, *Adv. Mater.*, 2020, **32**, 1904433.
24 S. Rai, A. Bajpai and S. Lokhandwala, *J. Polym.*, 2013, **2013**, 278576.
25 P. Thangasamy, S. Shanmuganathan and V. Subramanian, *Nanoscale Adv.*, 2020, **2**, 2073–2079.
26 J. Wang, W. Zhu, F. Meng, G. Bai, Q. Zhang and X. Lan, *ACS Catal.*, 2023, **13**, 4316–4329.
27 H. B. Yang, S.-F. Hung, S. Liu, K. Yuan, S. Miao, L. Zhang, X. Huang, H.-Y. Wang, W. Cai, R. Chen, J. Gao, X. Yang, W. Chen, Y. Huang, H. M. Chen, C. M. Li, T. Zhang and B. Liu, *Nat. Energy*, 2018, **3**, 140–147.
28 C. A. Trickett, A. Helal, B. A. Al-Maythalony, Z. H. Yamani, K. E. Cordova and O. M. Yaghi, *Nat. Rev. Mater.*, 2017, **2**, 17045.
29 G. Yang, S. Li, N. Li, P. Zhang, C. Su, L. Gong, B. Chen, C. Qu, D. Qi, T. Wang and J. Jiang, *Angew. Chem., Int. Ed.*, 2022, **61**, e202205585.
30 W. Liu, X. Li, C. Wang, H. Pan, W. Liu, K. Wang, Q. Zeng, R. Wang and J. Jiang, *J. Am. Chem. Soc.*, 2019, **141**, 17431–17440.
31 X.-K. Wang, J. Liu, L. Zhang, L.-Z. Dong, S.-L. Li, Y.-H. Kan, D.-S. Li and Y.-Q. Lan, *ACS Catal.*, 2019, **9**, 1726–1732.
32 H.-L. Zheng, S.-L. Huang, M.-B. Luo, Q. Wei, E.-X. Chen, L. He and Q. Lin, *Angew. Chem., Int. Ed.*, 2020, **59**, 23588–23592.
33 W. Chen, B. Han, C. Tian, X. Liu, S. Liang, H. Deng and Z. Lin, *Appl. Catal., B*, 2019, **244**, 996–1003.
34 B. Han, J. Song, S. Liang, W. Chen, H. Deng, X. Ou, Y.-J. Xu and Z. Lin, *Appl. Catal., B*, 2020, **260**, 118208.
35 B. Han, X. Ou, Z. Zhong, S. Liang, X. Yan, H. Deng and Z. Lin, *Appl. Catal., B*, 2021, **283**, 119594.

36 K. Song, S. Liang, X. Zhong, M. Wang, X. Mo, X. Lei and Z. Lin, *Appl. Catal., B*, 2022, **309**, 121232.
37 B. Han, X. Ou, Z. Deng, Y. Song, C. Tian, H. Deng, Y.-J. Xu and Z. Lin, *Angew. Chem., Int. Ed.*, 2018, **57**, 16811–16815.
38 L. Li, X. Dai, D.-L. Chen, Y. Zeng, Y. Hu and X. W. Lou, *Angew. Chem., Int. Ed.*, 2022, **61**, e202205839.
39 L. Tan, S.-M. Xu, Z. Wang, Y. Xu, X. Wang, X. Hao, S. Bai, C. Ning, Y. Wang, W. Zhang, Y. K. Jo, S.-J. Hwang, X. Cao, X. Zheng, H. Yan, Y. Zhao, H. Duan and Y.-F. Song, *Angew. Chem., Int. Ed.*, 2019, **58**, 11860–11867.
40 C. Gao, Q. Meng, K. Zhao, H. Yin, D. Wang, J. Guo, S. Zhao, L. Chang, M. He, Q. Li, H. Zhao, X. Huang, Y. Gao and Z. Tang, *Adv. Mater.*, 2016, **28**, 6485–6490.
41 S. Wang, Z. Ding and X. Wang, *Chem. Commun.*, 2015, **51**, 1517–1519.
42 M. Dong, J. Zhou, J. Zhong, H.-T. Li, C.-Y. Sun, Y.-D. Han, J.-N. Kou, Z.-H. Kang, X.-L. Wang and Z.-M. Su, *Adv. Funct. Mater.*, 2022, **32**, 2110136.
43 K.-Q. Lu, Y.-H. Li, F. Zhang, M.-Y. Qi, X. Chen, Z.-R. Tang, Y. M. A. Yamada, M. Anpo, M. Conte and Y.-J. Xu, *Nat. Commun.*, 2020, **11**, 5181.
44 J.-W. Wang, L.-Z. Qiao, H.-D. Nie, H.-H. Huang, Y. Li, S. Yao, M. Liu, Z.-M. Zhang, Z.-H. Kang and T.-B. Lu, *Nat. Commun.*, 2021, **12**, 813.
45 H.-X. Zhang, Q.-L. Hong, J. Li, F. Wang, X. Huang, S. Chen, W. Tu, D. Yu, R. Xu, T. Zhou and J. Zhang, *Angew. Chem., Int. Ed.*, 2019, **58**, 11752–11756.
46 K. Niu, Y. Xu, H. Wang, R. Ye, H. L. Xin, F. Lin, C. Tian, Y. Lum, K. C. Bustillo, M. M. Doeff, M. T. M. Koper, J. Ager, R. Xu and H. Zheng, *Sci. Adv.*, 2017, **3**, e1700921.
47 W. Zhong, R. Sa, L. Li, Y. He, L. Li, J. Bi, Z. Zhuang, Y. Yu and Z. Zou, *J. Am. Chem. Soc.*, 2019, **141**, 7615–7621.
48 W. Zhou, Q.-W. Deng, G.-Q. Ren, L. Sun, L. Yang, Y.-M. Li, D. Zhai, Y.-H. Zhou and W.-Q. Deng, *Nat. Commun.*, 2020, **11**, 4481.
49 J. Van Houten and R. J. Watts, *J. Am. Chem. Soc.*, 1976, **98**, 4853–4858.
50 Y. Su, Z. Song, W. Zhu, Q. Mu, X. Yuan, Y. Lian, H. Cheng, Z. Deng, M. Chen, W. Yin and Y. Peng, *ACS Catal.*, 2021, **11**, 345–354.
51 C. Gao, S. Chen, Y. Wang, J. Wang, X. Zheng, J. Zhu, L. Song, W. Zhang and Y. Xiong, *Adv. Mater.*, 2018, **30**, 1704624.
52 M. Hartmann, N. Azuma and L. Kevan, *J. Phys. Chem. C*, 1995, **99**, 10988–10994.
53 W. Ma, S. Xie, T. Liu, Q. Fan, J. Ye, F. Sun, Z. Jiang, Q. Zhang, J. Cheng and Y. Wang, *Nat. Catal.*, 2020, **3**, 478–487.
54 G. Qian, W. Lyu, X. Zhao, J. Zhou, R. Fang, F. Wang and Y. Li, *Angew. Chem., Int. Ed.*, 2022, **61**, e202210576.
55 S. Jiao, X. Fu and H. Huang, *Adv. Funct. Mater.*, 2022, **32**, 2107651.
56 Y. Wang, N.-Y. Huang, J.-Q. Shen, P.-Q. Liao, X.-M. Chen and J.-P. Zhang, *J. Am. Chem. Soc.*, 2018, **140**, 38–41.
57 W. Chen, X. Liu, B. Han, S. Liang, H. Deng and Z. Lin, *Nano Res.*, 2021, **14**, 730–737.
58 S. Liang, X. Liu, Z. Zhong, B. Han, X. Zhong, W. Chen, K. Song, H. Deng and Z. Lin, *Nano Res.*, 2021, **14**, 2558–2567.
59 P. D. C. Dietzel, R. E. Johnsen, H. Fjellvag, S. Bordiga, E. Groppo, S. Chavan and R. Blom, *Chem. Commun.*, 2008, 5125–5127.

